RESEARCH ARTICLE
SPACE PHYSICS: MAGNETOSPHERIC PHYSICS

Earth and Planetary Physics
7: 620–630, 2023
doi: 10.26464/epp2023079

A data assimilation-based forecast model of outer radiation belt electron fluxes

Yuan Lei[1], Xing Cao[1*], BinBin Ni[1,2*], Song Fu[1], TaoRong Luo[1], and XiaoYu Wang[1]

[1]Department of Space Physics, School of Electronic Information, Wuhan University, Wuhan 430072, China;

[2]Chinese Academy of Sciences Center for Excellence in Comparative Planetology, Hefei 230026, China

Key Points:

- A forecast model based on data assimilation is developed to predict electron fluxes in the outer radiation belt over a wide range of electron pitch angle and energy.
- Our model reasonably predicts the storm-time evolution of radiation belt electrons.
- The best prediction performance is found for ~0.3–3 MeV electrons at L = ~3.25–4.5, which extends to lower energies and higher L with increasing pitch angle.

Citation: Lei, Y., Cao, X., Ni, B. B., Fu, S., Luo, T. R., and Wang X. Y. (2023). A data assimilation-based forecast model of outer radiation belt electron fluxes. *Earth Planet. Phys.*, *7*(6), 620–630. http://doi.org/10.26464/epp2023079

Abstract: Because radiation belt electrons can pose a potential threat to the safety of satellites orbiting in space, it is of great importance to develop a reliable model that can predict the highly dynamic variations in outer radiation belt electron fluxes. In the present study, we develop a forecast model of radiation belt electron fluxes based on the data assimilation method, in terms of Van Allen Probe measurements combined with three-dimensional radiation belt numerical simulations. Our forecast model can cover the entire outer radiation belt with a high temporal resolution (1 hour) and a spatial resolution of 0.25 L over a wide range of both electron energy (0.1–5.0 MeV) and pitch angle (5°–90°). On the basis of this model, we forecast hourly electron fluxes for the next 1, 2, and 3 days during an intense geomagnetic storm and evaluate the corresponding prediction performance. Our model can reasonably predict the storm-time evolution of radiation belt electrons with high prediction efficiency (up to ~0.8–1). The best prediction performance is found for ~0.3–3 MeV electrons at L = ~3.25–4.5, which extends to higher L and lower energies with increasing pitch angle. Our results demonstrate that the forecast model developed can be a powerful tool to predict the spatiotemporal changes in outer radiation belt electron fluxes, and the model has both scientific significance and practical implications.

Keywords: Earth's outer radiation belt; data assimilation; electron flux forecast; model performance evaluation

1. Introduction

The Earth's outer radiation belt consists of high-energy electrons (~100 keV–10 MeV) trapped by the geomagnetic field and is located at L-shell = ~3–7. A majority of medium- and high-orbit satellites pass through the region covered by the outer belt, where the electrons can undermine spacecraft electronics via deep-dielectric charging and discharging phenomena. The outer belt electron fluxes are usually characterized by complex and intense dynamics as a result of the imbalance between acceleration, loss, and transport processes (Ni BB et al., 2013a, 2015, 2022; Baker et al., 2014; Fu S et al., 2020; Mei Y et al., 2021; Wang CQ et al., 2021). Resonant interactions with plasma waves are recognized as playing a crucial role in the dynamic evolution of radiation belt electrons (Thorne, 2010). A series of studies have demonstrated that many plasma waves, such as electromagnetic ion cyclotron (EMIC) waves, magnetosonic waves, whistler-mode chorus waves, and plasmaspheric hiss, can effectively affect the radiation belt electron dynamics via pitch angle and energy diffusion (Summers et al., 2003; Thorne et al., 2007, 2013; Hudson et al., 2008; Fu HS et al., 2011; Reeves et al., 2013; Xiao FL et al., 2014, 2015; Ni BB et al., 2016, 2017, 2019, 2023a, b; Li LY et al., 2016; Cao X et al., 2017a, b, 2020a, 2023; Zong QG et al., 2017; Fu S et al., 2019; Zhang DJ et al., 2020; Capannolo et al., 2021; Zhu, MH et al., 2022; He, F et al., 2023).

Satellite measurements provide an effective means for understanding the radiation belt electron dynamics. However, they are usually limited to a restricted coverage of L-shell, electron energy, and pitch angle. By solving the three-dimensional (3-D) Fokker–Planck diffusion equation, various numerical models have been developed to simulate the dynamics of radiation belt electrons, including the Salammbô code (Beutier and Boscher, 1995), Versatile Electron Radiation Belt (VERB)-3D code (Shprits et al., 2009), Storm-Time Evolution of Electron Radiation Belt (STEERB) code (Su ZP et al., 2010), Dynamic Radiation Environment Assimi-

First author: Y. Lei, yuan.lei@whu.edu.cn
Correspondence to: X. Cao, cxing@whu.edu.cn
B. B. Ni, bbni@whu.edu.cn
Received 13 JUL 2023; Accepted 30 AUG 2023.
First Published online 15 SEP 2023.
©2023 by Earth and Planetary Physics.

lation Model (DREAM)-3D code (Tu WC et al., 2013), British Antarctic Survey (BAS) Radiation Belt code (Glauert et al., 2014), and University of California, Los Angeles (UCLA)-3D code (Ma Q et al., 2015). However, radiation belt numerical models still possess some unavoidable shortcomings, such as simplification treatment in solving equations and inaccurate initial and boundary conditions.

Data assimilation (DA) techniques are able to combine numerical models and observation data, taking into account the inherent errors of both separately, to optimally estimate the true state of the system. Therefore, data assimilation has been widely used in the radiation belt community to reconstruct the spatial and temporal distribution of radiation belt electrons. The available data assimilation algorithms that are used in radiation belt research consist of the Kalman filter (KF; e.g., Shprits et al., 2007, 2012, 2013; Ni BB et al., 2009a, b, 2013b; Daae et al., 2011; Schiller et al., 2012; Kellerman et al., 2014; Zhu JN et al., 2021), extended Kalman filter (EKF; e.g., Naehr et al., 2005; Kondrashov et al., 2007, 2011), and ensemble Kalman filter (EnKF; e.g., Koller et al., 2007; Godinez and Koller, 2012; Reeves et al., 2012; Yu Y et al., 2014; Tibocha et al., 2021).

To ensure the safety of spacecraft, various models have been developed in previous studies to forecast the evolution of energetic electrons at Geostationary Earth Orbit (GEO). Through linear prediction filter analysis, Baker et al. (1990) predicted radiation belt electron fluxes using the geomagnetic or solar wind indices as inputs. This method was subsequently implemented to develop the relativistic electron forecast model operating at the Space Weather Prediction Center (SWPC). Kellerman et al. (2013) developed a prediction model of radiation belt electron fluxes based on the measurements of solar wind parameters to forecast relativistic electron fluxes at GEO. In addition, the nonlinear processes of electron flux variations have been considered. Boynton et al. (2016) developed an empirical model based on the Nonlinear Autoregressive Moving Average with Exogenous inputs (NARMAX) algorithm to predict geosynchronous electron fluxes. Recently, the neural network technique has been extensively utilized in predicting electron fluxes in the radiation belts (Ling AG et al., 2010; Shin et al., 2016; Wei LH et al., 2018; Zhang H et al., 2020; Son et al., 2022; Tang RX et al., 2022; Wing et al., 2022; Wang JH et al., 2023).

Prediction models also exist that can predict variations in the outer radiation belt electron fluxes over a wide spatial range. Rigler et al. (2004) used the KF to recursively update the linear prediction filter coefficients for the prediction of relativistic electron fluxes. Coleman et al. (2018) developed a nowcast model of 2.1 MeV electron fluxes at L = 3–6 by using a time-varying linear filter. Chen Y et al. (2019) developed the PREdictive models for MeV Electrons (PreMevE) by using a linear prediction filter, which can predict megaelectron volt electron fluxes at L = 2.8–7 with low-orbit satellite data as inputs. Combining machine learning algorithms, de Lima et al. (2020) subsequently upgraded PreMevE to provide improved predictions of megaelectron-volt electron fluxes. However, the aforementioned models focus only on the prediction of electron fluxes at a specific energy or the integral fluxes.

In this work, we reconstruct the distribution of electron fluxes in the outer radiation belt, using the KF method by combining Van Allen Probe observations and 3-D radiation belt numerical modeling. We further develop a forecast model of electron fluxes covering a wide range of electron energy (0.1–5 MeV) and L^* (3–7). We have organized this manuscript as follows: Van Allen Probe instruments and the data set used are briefly described in Section 2. Section 3 briefly introduces our algorithms and models. The forecasted results and performance evaluations of this model are presented in Section 4. Finally, the main conclusions of this study are summarized in Section 5.

2. Instrumentation and Data

In the present study, we adopt high-quality electron data observed by the identical twin Van Allen Probes during the period from April to May 2017. Their orbits are characterized by a low inclination (~10°), a perigee of ~1.1 R_E (Earth's radius) and an apogee of ~5.9 R_E, with a period of ~9 h (Mauk et al., 2013). The electron data used in this study are measured by two in situ instrumentations: the Magnetic Electron Ion Spectrometer (MagEIS) instrumentation and the Relativistic Electron Proton Telescope (REPT) instrumentation. The MagEIS instrumentation covers an energy range of ~30 keV–4 MeV in 21 energy channels, and the REPT instrumentation covers an energy range of ~1.8–20 MeV in 12 energy channels. The corresponding pitch angles detected by MagEIS and REPT are ~8° to 172° and ~5° to 175°, respectively.

3. Model Description

3.1 Radiation Belt Modeling

The spatial and temporal evolution of radiation belt electron phase space density (PSD) can be obtained by solving the 3-D Fokker–Planck equation in the coordinates of three adiabatic invariants (μ, K, L^*; Schulz and Lanzerotti, 1974):

$$\frac{\partial f}{\partial t} = L^{*2}\frac{\partial}{\partial L^*}\bigg|_{\mu,K}\left(\frac{1}{L^{*2}}D_{L^*L^*}\frac{\partial f}{\partial L^*}\bigg|_{\mu,K}\right) + \frac{1}{p^2}\frac{\partial f}{\partial p}\bigg|_{\alpha_0,L^*}p^2\left(D_{pp}\frac{\partial f}{\partial p}\bigg|_{\alpha_0,L^*}\right) + \frac{1}{T(\alpha_0)\sin(2\alpha_0)}\frac{\partial}{\partial \alpha_0}\bigg|_{p,L^*}T(\alpha_0)\sin(2\alpha_0)\left(D_{\alpha_0\alpha_0}\frac{\partial f}{\partial \alpha_0}\bigg|_{p,L^*}\right) - \frac{f}{\tau}, \tag{1}$$

where f is the electron PSD, p is the relativistic momentum, α_0 is the equatorial pitch angle, $T(\alpha_0)$ is the normalized bounce period, and τ is the electron lifetime. If inside the loss cone, τ is a quarter of the bounce period; otherwise, it is infinity. In addition, $D_{\alpha_0\alpha_0}$, D_{pp}, and $D_{L^*L^*}$ denote the bounce-averaged pitch angle, momentum diffusion rates, and radial diffusion coefficients, respectively.

In this study, we obtain $D_{L^*L^*}$ from Brautigam and Albert (2000). In addition, we include the contributions from chorus waves and plasmaspheric hiss by calculating the pitch angle and momentum scattering rates using the Full Diffusion Code (FDC; Ni BB et al., 2008, 2015; Shprits et al., 2009; Cao X et al., 2016, 2020a, b), with the corresponding wave parameters adopted from Li W et al. (2007). The plasmapause position is obtained based on the study by Carpenter and Anderson (1992).

3.2 Kalman Filter Algorithm

The KF, a sequential data assimilation method, allows us to consider the error level of different measurements and a physics-

based model and optimally combine the measurements and the model. In this study, the KF is applied to obtain an optimal estimate of radiation belt electron fluxes.

Assuming the dynamic process of the electron PSD evolution described by the 3-D Fokker–Planck equation can be represented by the numerically discretized form:

$$\boldsymbol{x}_k^f = \boldsymbol{M}_{k-1}\boldsymbol{x}_{k-1}^a, \tag{2}$$

where $\boldsymbol{x}$ represents the PSD state vector and superscripts f and a indicate the forecast value and analysis value, respectively. The state matrix $\boldsymbol{M}$ is the 3-D Fokker–Planck discretized numerical model. If the model error is considered here, the evolution of the true PSD value can be determined by

$$\boldsymbol{x}_k^t = \boldsymbol{M}_{k-1}\boldsymbol{x}_{k-1}^t + \eta_{k-1}^m, \tag{3}$$

where superscript t refers to true, and η_{k-1}^m is the model error and is assumed to be a white Gaussian noise with zero mean and error covariance $\boldsymbol{Q}_{k-1}$. Therefore, the forecast error covariance $\boldsymbol{P}_k^f$ is represented by

$$\boldsymbol{P}_k^f = \boldsymbol{M}_{k-1}\boldsymbol{P}_{k-1}^a\boldsymbol{M}_{k-1}^{\mathrm{T}} + \boldsymbol{Q}_{k-1}, \tag{4}$$

where $\boldsymbol{P}_{k-1}^a$ is the error covariance of the analysis value at time $k-1$. The observations $\boldsymbol{y}_k^o$ are also assumed to have as error a white Gaussian noise $\boldsymbol{\varepsilon}_k^o$ with zero mean and the observational error covariance $\boldsymbol{R}_k$:

$$\boldsymbol{y}_k^o = \boldsymbol{H}_k\boldsymbol{x}_k^t + \boldsymbol{\varepsilon}_k^o, \tag{5}$$

where superscript o indicates observation and $\boldsymbol{H}_k$ is the observation matrix composed of 0 and 1 elements. Because the sparsity of actual satellite measurements results in fewer dimensions of the observations than the modeled values, $\boldsymbol{H}_k$ is constructed to map the forecasted values onto observed space.

The vector of observations and the vector of the forecast state are used to obtain the analysis state vector $\boldsymbol{x}_k^a$,

$$\boldsymbol{x}_k^a = \boldsymbol{x}_k^f + \boldsymbol{K}_k\left(\boldsymbol{y}_k^o - \boldsymbol{H}_k\boldsymbol{x}_k^f\right), \tag{6}$$

where the Kalman gain $\boldsymbol{K}_k$ enables the error covariance $\boldsymbol{P}_k^a$ of the optimal estimate to minimize:

$$\boldsymbol{K}_k = \boldsymbol{P}_k^f\boldsymbol{H}_k^{\mathrm{T}}\left(\boldsymbol{H}_k\boldsymbol{P}_k^f\boldsymbol{H}_k^{\mathrm{T}} + \boldsymbol{R}_k\right)^{-1}, \tag{7}$$

$$\boldsymbol{P}_k^a = \left(\boldsymbol{I} - \boldsymbol{K}_k\boldsymbol{H}_k\right)\boldsymbol{P}_k^f. \tag{8}$$

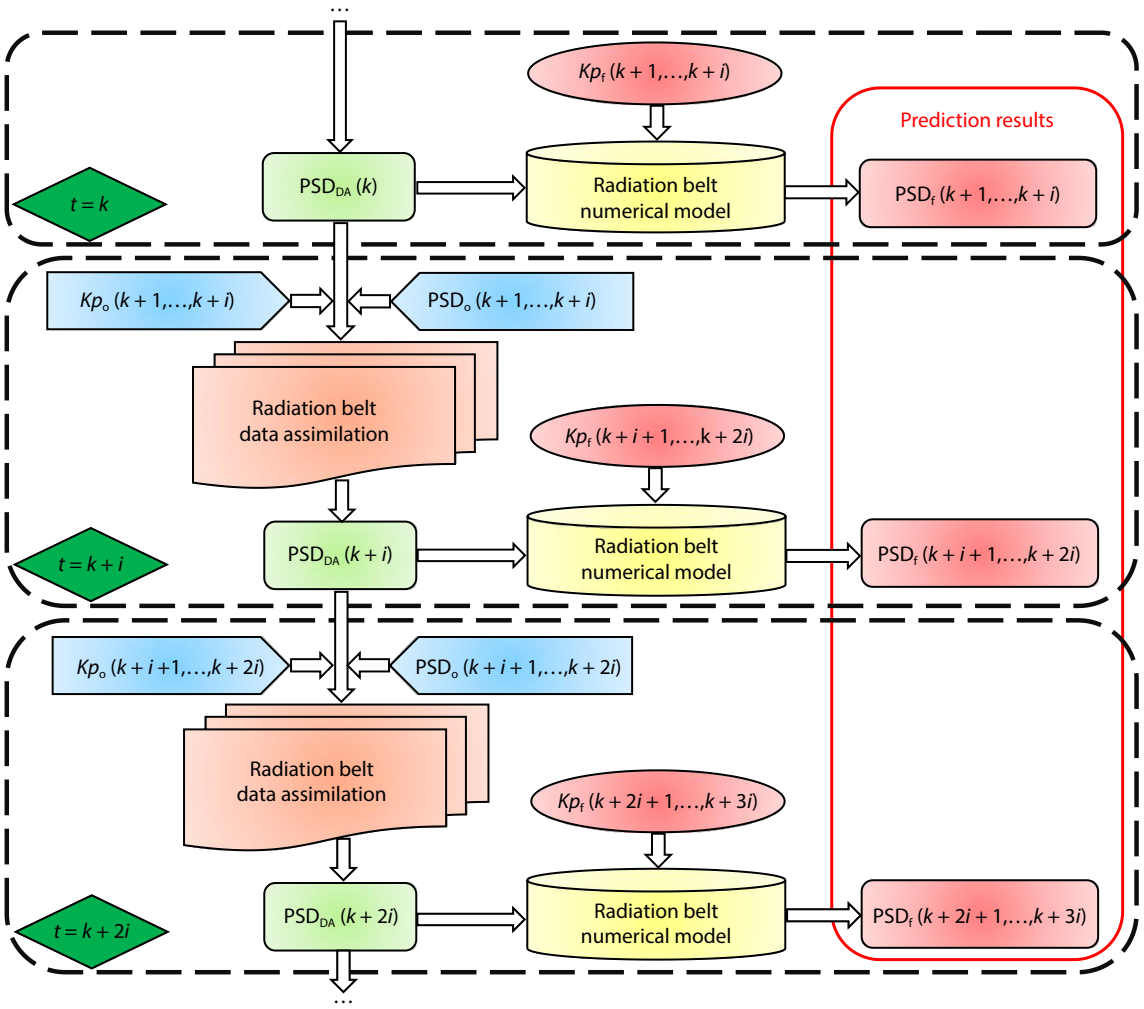

Figure 1. The forecast flowchart of radiation belt electron fluxes. PSD_f, PSD_o, and PSD_{DA} represent the forecasted, observed, and assimilative electron PSD, respectively. Kp_f and Kp_o are the forecasted and observed Kp indices.

3.3 Forecast Flowchart

In this study, we predict electron fluxes for the next *i* hours, and we assume that electron flux and *Kp* observations will be received every *i*th hour during this period. This process can be divided into (1) **the forecast process** and (2) **the assimilation process**. The main steps in forecasting electron fluxes are as follows:

(1) **Forecast process.** The assimilative results of electron PSD at $t = k$ is used as the initial value for forecast. Then, the forecasted value of *Kp* for each hour in the future, *i* hours, is input into the numerical model to obtain the forecasted value of PSD for each hour in the future *i* hours, respectively.

(2) **Assimilation process.** After *i* hours, namely $t = k + i$, the PSD observations and *Kp* observations for the past *i* hours are received. Then, the PSD assimilative value at $t = k$ is used as the initial value for assimilation to obtain the PSD assimilative value at the current moment, which is then used as the initial value for the forecast of the next forecast period.

As time advances, the process of forecasting and assimilation is continuously cycled, and the forecast of electron fluxes is realized for the whole time period. Note that the forecasted value of *Kp* is replaced by its real value, the results of measurement in this study. Our forecast model is able to predict the radiation belt electron fluxes hourly with a spatial resolution of 0.25 L^* at $L^* = 3$–7 in the pitch angle range of 5°–90° and the energy range of 0.1–5 MeV.

4. Model Results

Usually, a period of runs is required to achieve the optimal model performance when reconstructing electron fluxes using the data assimilation method. Therefore, we first reconstruct the electron fluxes in April 2017 to stabilize the assimilation model, and then predict the electron fluxes in May 2017 for the next 1, 2, and 3 days, respectively.

Figure 2 shows the observed and forecasted electron fluxes for different electron energies and forecast times at a fixed $\alpha_{eq} = 30°$. Figure 2a illustrates the *Kp* and *Dst* indices. Figures 2b–2e and 2f–2i show the results for $E_k = 0.5$ and 1 MeV, respectively. The observed electron fluxes are shown in Figures 2b and 2f, and the assimilative electron fluxes in April 2017 and the forecasted electron fluxes in May 2017 for the next 1, 2, and 3 days are shown in Figures 2c–2e and 2g–2i. The data assimilation results not only fill the gaps in the observations, but also accurately reconstruct the radial profiles and the evolution of the electron fluxes. The assimilative results are used as initial conditions for model prediction. It can be seen that the 1-day forecast for $E_k = 0.5$ MeV in Figure 2c can well predict the process of radiation belt electrons in May 2017, including the prompt enhancement of electron fluxes after the intense geomagnetic storm occurred on May 28, although the electron dropout at high L^* during the main phase is not captured well. The forecasted results for the electron fluxes at $E_k = 0.5$ MeV for the 2- and 3-day forecasts generally agree well with the observations, but the discrepancies become pronounced with the extension of forecast time. Compared with 0.5 MeV electrons, the forecasted results for 1 MeV electrons are closer to the observations. Note that as the prediction time increases, the model prediction performance for 1 MeV electrons is more stable than that for 0.5 MeV electrons.

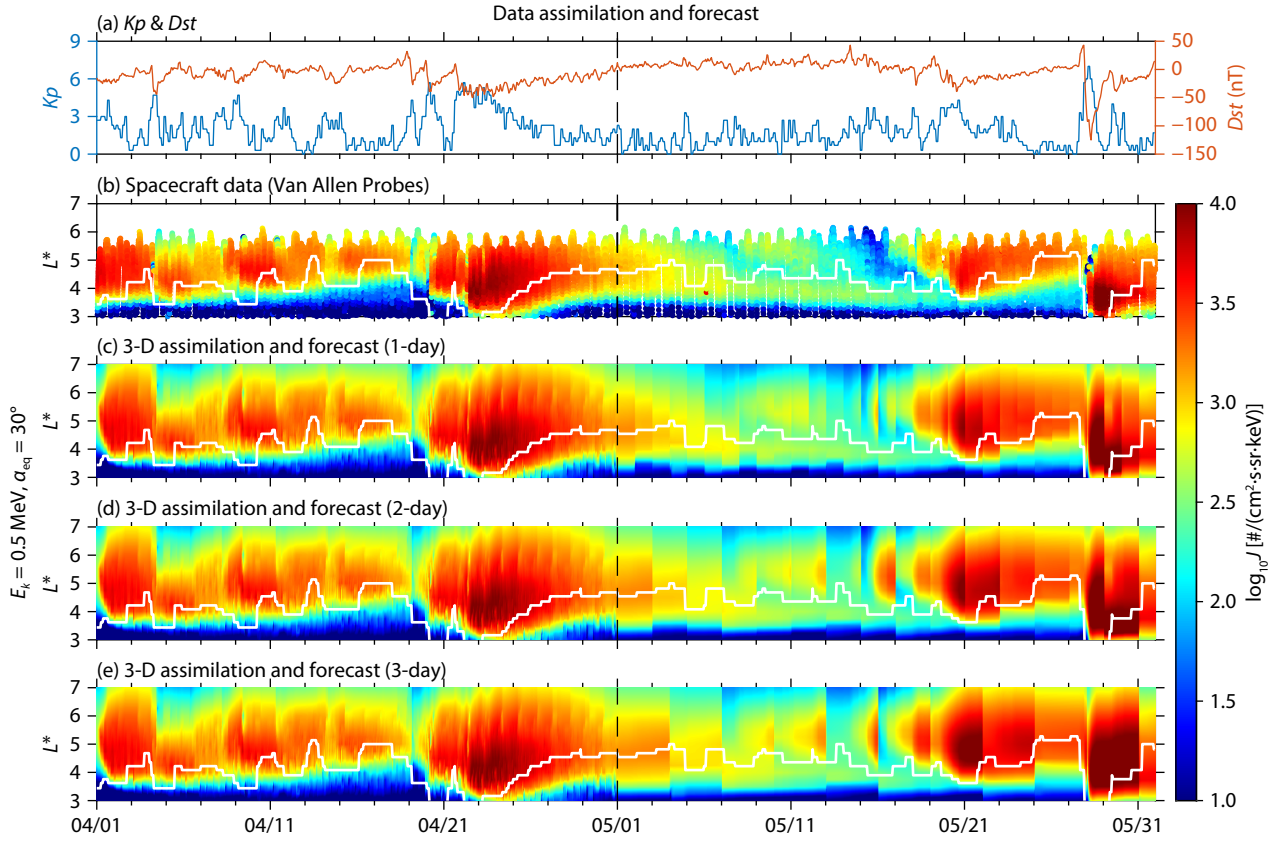

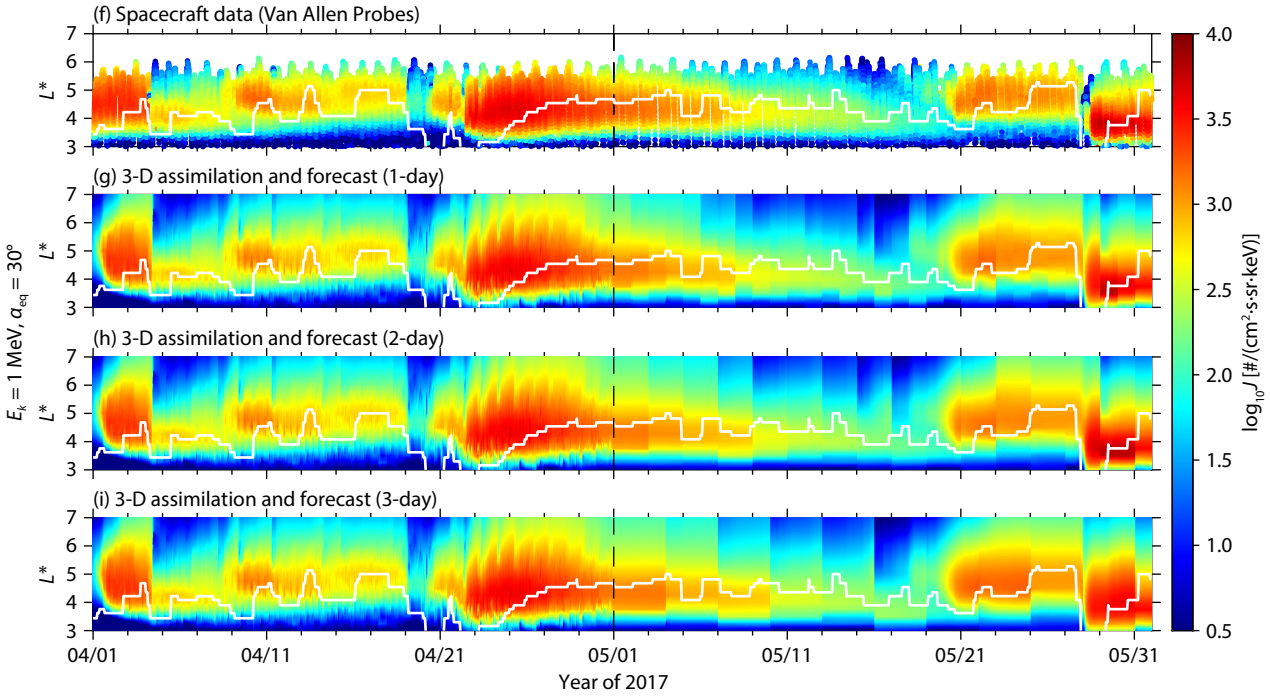

Figure 2. (a) *Kp* and *Dst* indices. (b) Van Allen Probe observations of electron fluxes at E_k = 0.5 MeV and α_{eq} = 30° from April 1 to May 31, 2017. (c–e) Assimilative electron fluxes in April 2017 and forecasted electron fluxes in May 2017 for E_k = 0.5 MeV and α_{eq} = 30° electrons for 1-, 2-, and 3-day forecasts, respectively. (f–i) Observed, assimilative, and forecasted electron fluxes for E_k = 1 MeV and α_{eq} = 30° electrons. The white line in panels b–i represents the position of the plasmapause. The vertical dashed line in each panel represents the start of prediction.

In Figure 3, we further show the observed and forecasted electron fluxes for E_k = 2 and 5 MeV electrons at α_{eq} = 60°. The figure shows that the assimilative results generally reproduce the distribution of 2 and 5 MeV electrons at L^* = 3–7 in April 2017. On the basis of the assimilative results in April, our model subsequently predicts the evolution of electron fluxes for E_k = 2 and 5 MeV electrons. We can see that the prediction for 2 MeV electrons is closer to the observations than is the prediction for 5 MeV electrons. Especially during the strong geomagnetic storm on May 28, the predicted fluxes of 5 MeV electrons are much higher than the observations. This result may be attributed to the absence of the EMIC wave-induced loss of ultrarelativistic electrons (Ni BB et al., 2015; Cao X et al., 2017c, 2020b).

Figure 4 illustrates the comparison between the observed and forecasted electron fluxes for different electron energies and pitch angles in May 2017 at L^* = 3.5, 4.5, and 5.5. Figures 4a–4f show the results for 0.5 and 1 MeV electrons at α_{eq} = 30°, and Figure 4g–4l show the results for 2 and 5 MeV electrons at α_{eq} = 60°. The green circles in each panel indicate the observations. The black, blue, and red lines represent forecasted electron fluxes for 1-, 2-, and 3-day forecasts, respectively. We can see that compared with the 1 and 2 MeV electrons, the discrepancies between the observed and forecasted fluxes of 0.5 and 5 MeV electrons are more pronounced. The forecasted results at L^* = 4.5 are found to be closer to the observations than are those at L^* = 3.5 and 5.5, except for 0.5 MeV electrons at α_{eq} = 30°. In addition, 0.5 and 5 MeV electron fluxes are found to be seriously overestimated after the geomagnetic storm.

To quantitatively evaluate our model performance, the mean error (ME), root mean squared error (RMSE), and prediction efficiency (PE) are calculated, which are given by

$$\mathrm{ME} = \frac{1}{N}\sum_{i=1}^{N}(f_i - o_i), \tag{9}$$

$$\mathrm{RMSE} = \sqrt{\frac{1}{N}\sum_{i=1}^{N}(f_i - o_i)^2}, \tag{10}$$

$$\mathrm{PE} = 1 - \frac{\sum_{i=1}^{N}(f_i - o_i)^2}{\sum_{i=1}^{N}(o_i - \langle o\rangle)^2} = 1 - \frac{\mathrm{RMSE}^2}{\mathrm{Var}\,(o)}. \tag{11}$$

where f_i is the forecasted results, o_i is the observed results, N refers to the total number of data points, and $\langle o\rangle$ and $\mathrm{Var}\,(o)$ are the mean and variance of all the observed results. Both ME and RMSE are used to evaluate the error of predicted results relative to the observations. However, ME can analyze whether the forecasted results are overestimated or underestimated, whereas RMSE is more sensitive to the magnitude of the differences. Prediction efficiency can be computed by the combination of RMSE and $\mathrm{Var}\,(o)$. Prediction efficiency denotes the relative accuracy of the forecasted results compared with the mean of the observations.

To estimate the performance of our model for predicting electron fluxes, Figure 5 shows the results of ME, RMSE, and PE as a function of electron energy and L^* for 1-day forecast corresponding to α_{eq} = 30°, 60°, and 80°. Figures 5a–5c show that <0.3 MeV electron fluxes are underestimated at L^* < 4 and overestimated at L^* > 4.5. For >3 MeV electrons, their fluxes are overestimated at L^* > 4.5. This result is consistent with Figures 5d–5f, which show that the RMSE in these areas are more obvious than others. We suggest that the discrepancies at low L^* may be caused by the inaccurate

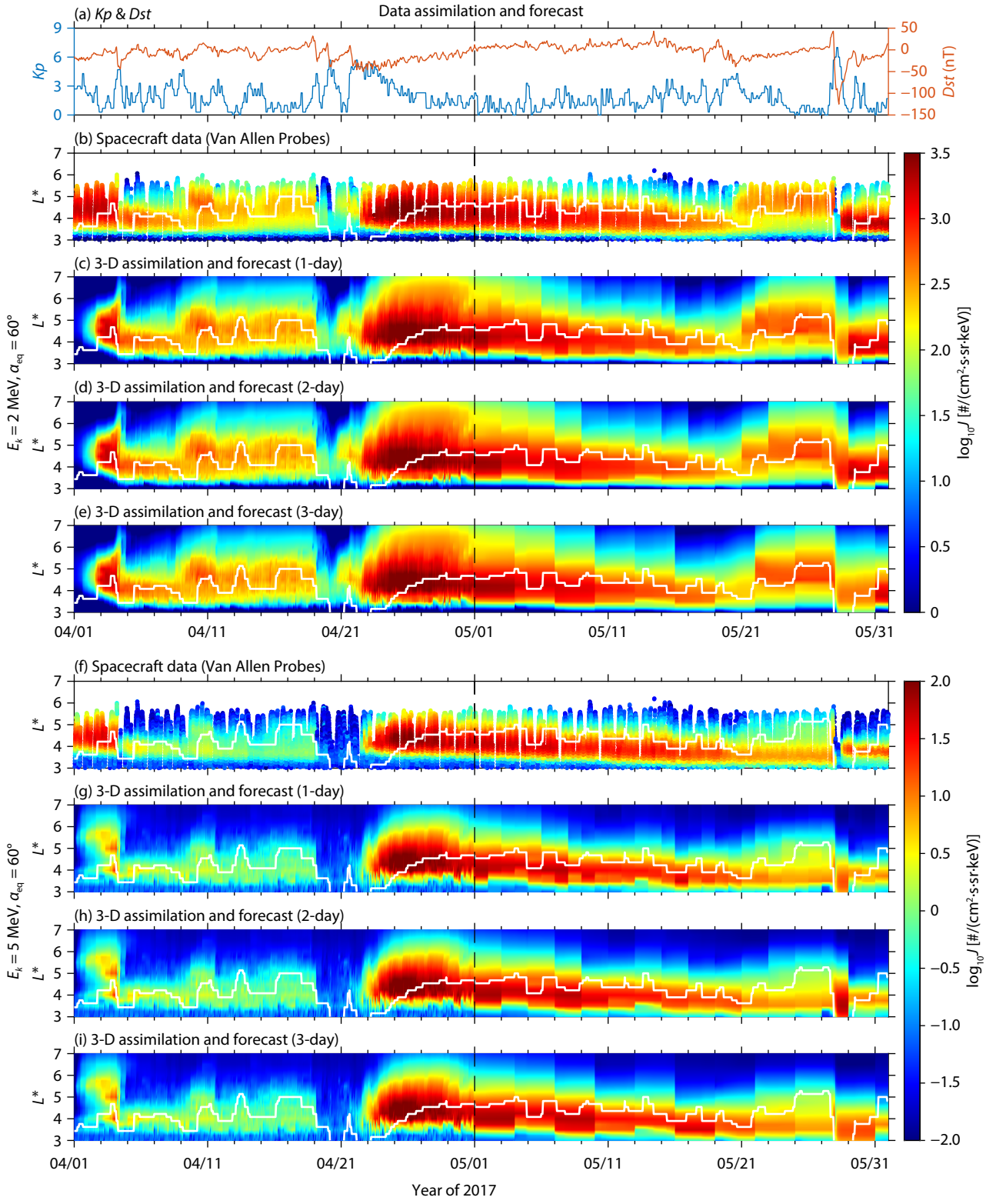

Figure 3. Same as Figure 2, except for E_k = 2 and 5 MeV electrons at α_{eq} = 60°.

empirical model of plasmaspheric hiss and the inaccurate position of plasmapause in our model. The overestimations at high L^* may have originated from the absence of electron loss resulting from EMIC wave scattering and magnetopause shadowing affects (Xiang Z et al., 2017, 2018). Figure 5d clearly illustrates that the RMSE of the model for < ~0.7 MeV electron fluxes at ~L^* = 5–5.25 is more pronounced than at other L^*. We suggest that this may be attributed to the fact that the electron dropout is poorly predicted by our model during this intense geomagnetic storm event on May 28. The RMSE indicates the absolute difference between predicated and observed values, yet this is often an inaccurate measure of the prediction performance of the model for different

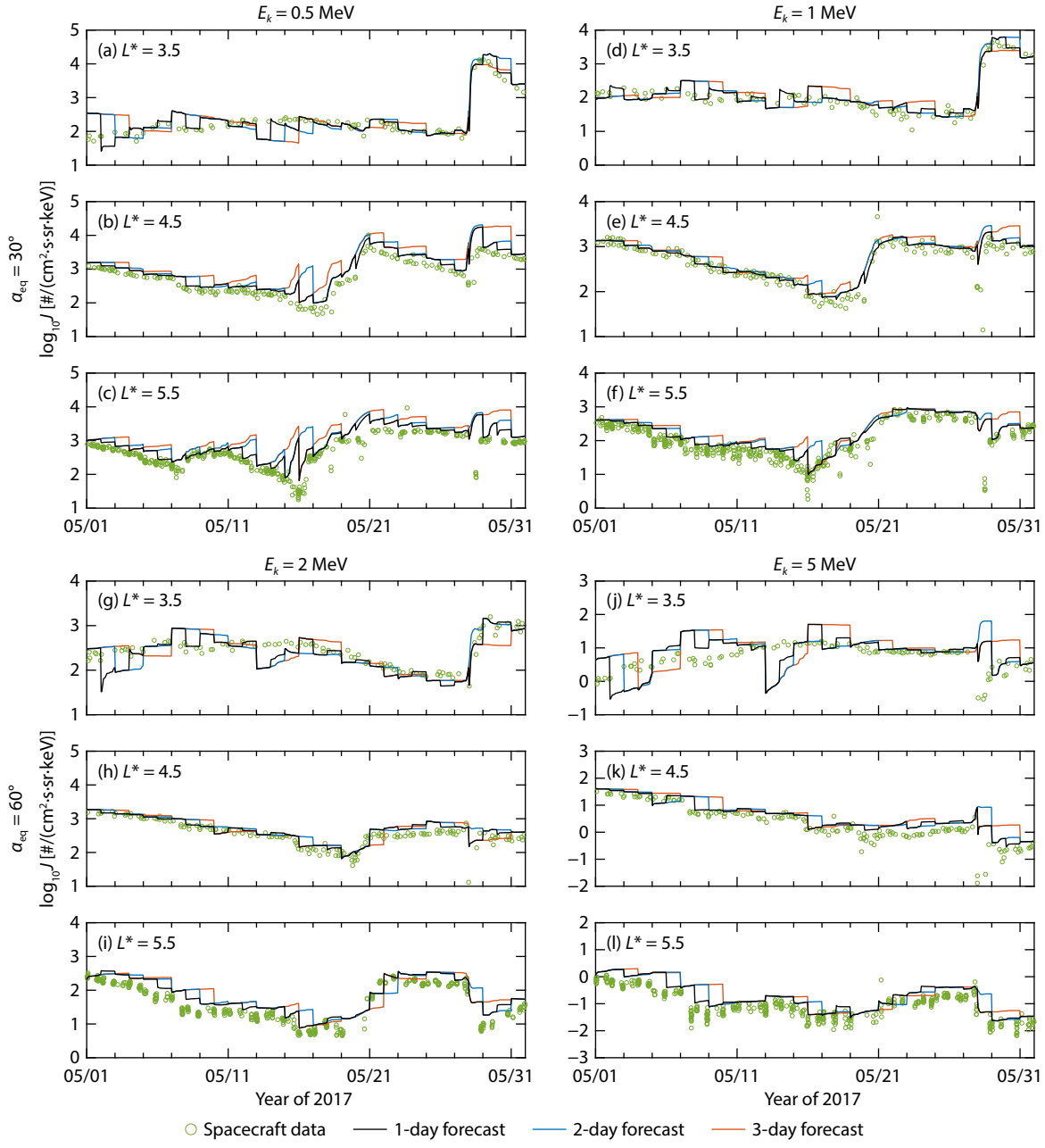

Figure 4. Comparison between observed and forecasted electron fluxes for different electron energies and pitch angles for 1-, 2-, and 3-day forecasts at L^* = 3.5, 4.5, and 5.5. The green circles in each panel indicate the observations. The black, blue, and red lines represent forecasted electron fluxes for 1-, 2-, and 3-day forecasts, respectively.

datasets because of the large differences in magnitude between the electron fluxes at different energies and L^*. It is thus more appropriate to use PE to compare our model performance for the electron flux prediction at different energies and L^*. Figures 5g–i show high PE (~0.7–1) for 0.3–3 MeV electrons at L^* = ~3.25–4.5, which gradually extends to higher L^* and lower energies with increasing pitch angle. Note that PE is significantly decreased for ~2.5 MeV electrons with increasing electron energies. Lower PE for higher energy electrons also may be a result of the missing scattering effects of EMIC waves on electrons in our forecast model. The dependence of our model performance on different prediction times is further shown in Figure 6. The figure shows that as the prediction time increases, the model performance gradually declines, regardless of electron energy and L^*.

Son et al. (2022) developed a deep learning model to predict the fluxes of >2 MeV electrons at GEO and PE for 1, 2, and 3 days ahead predictions were 0.78, 0.64, and 0.53, respectively. Although PE at GEO in our model is not available because of the absence of satellite measurements, Figure 5 shows that our model performance for ~0.3–3 MeV electrons at L^* = ~3.25–4.5 is comparable or even better than that of Son et al. (2022). We also compare it with the prediction performance of the PreMevE model (Chen Y et al., 2019). We find that the PE of our forecast model for 1 MeV electrons is lower than the PreMevE (with the peak PE higher than 0.8 at L = ~3.5) at α_{eq} = 30° but higher than the PreMevE at $\alpha_{eq} \geq 60°$.

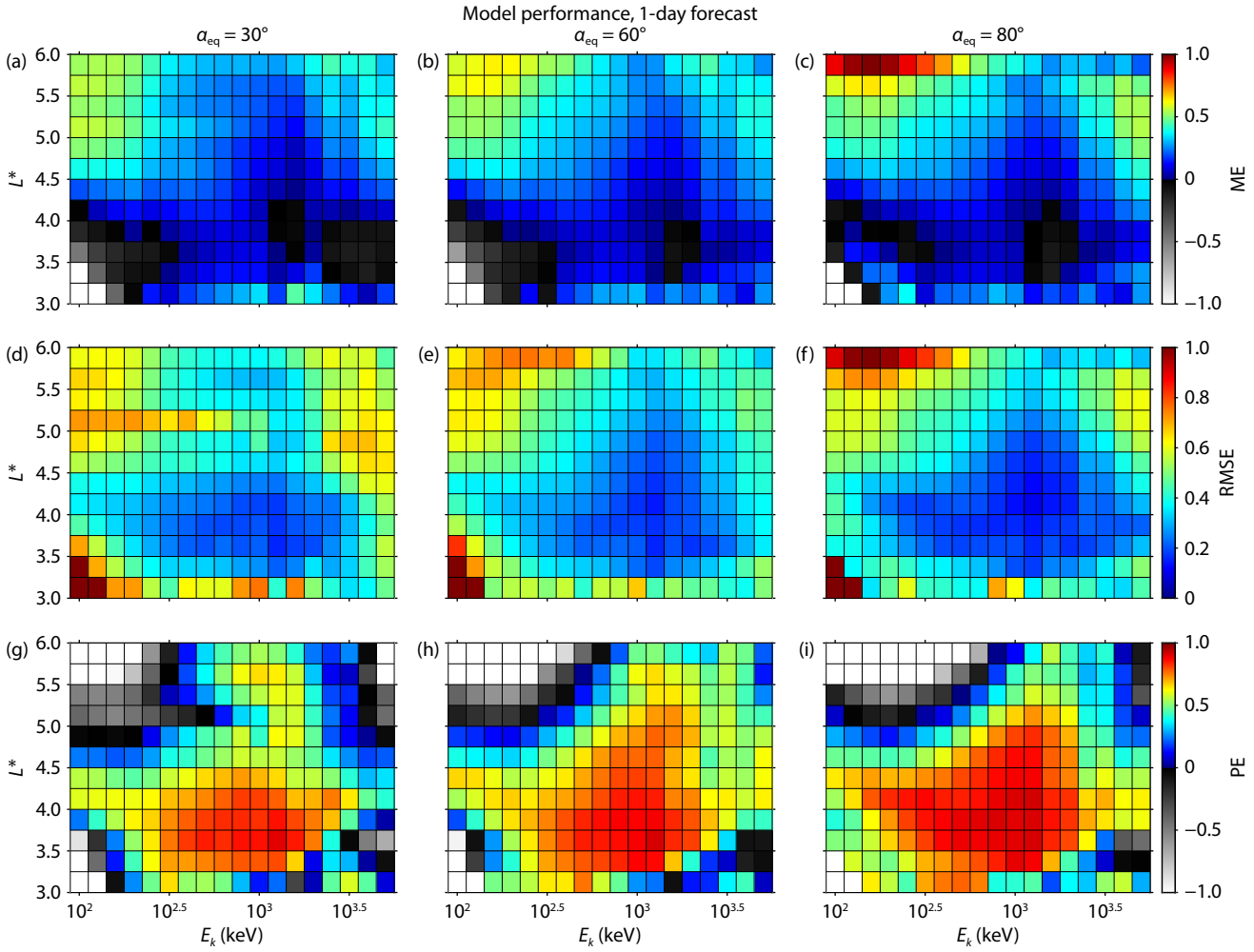

Figure 5. Distribution of three performance metrics (ME, RMSE, and PE) as a function of electron energy and L^* and for 1-day forecast corresponding to α_{eq} = 30°, 60°, and 80°.

5. Summary and Discussion

In this study, a forecast model of outer radiation belt electron fluxes is developed based on a data assimilation technique through the combination of Van Allen Probes measurements and 3-D radiation belt numerical simulations. Our model is able to predict electron fluxes with high temporal (1 hour) and spatial (0.25 L) resolutions over a wide electron energy range (0.1–5 MeV) and pitch angle range (5°–90°). We forecast radiation belt electron fluxes for the next 1, 2, and 3 days based on this model and evaluate the corresponding prediction performance.

The main conclusions can be summarized as follows:

(1) The data assimilation method can optimally estimate the current state of electron fluxes as the initial values for model prediction. Further, our model can reasonably forecast hourly electron fluxes for the next 1, 2, and 3 days, with high PE above ~0.8.

(2) Compared with previous studies, our model not only has good prediction performance, but also can predict radiation belt electron fluxes (L^* = 3–7) in the outer belt over a wider pitch angle (5°–90°) and energy range (0.1–5 MeV).

(3) Our model has the best prediction performance (up to ~0.8–1) for electron fluxes at E_k = ~0.3–3 MeV and L^* = ~3.25–4.5, which gradually extends to higher L^* and lower energies with increasing pitch angle. In addition, the prediction performance becomes more robust as the prediction time decreases.

In this study, we consider only the resonant scattering of radiation belt electrons by whistler-mode chorus waves and plasmaspheric hiss. It is of future interest to include the contributions of other plasma waves (e.g., magnetosonic waves, EMIC waves) to the acceleration and loss processes of radiation belt electrons in our forecast model. Specifically, because EMIC waves can effectively cause the pitch angle scattering loss of relativistic electrons, the absence of EMIC waves in our model will result in the overestimation of relativistic electron fluxes. In addition, magnetopause shadowing effects, which are a crucial mechanism responsible for the loss of electrons, should be taken into account. For simplicity, the observed Kp is used for forecasting radiation belt electron fluxes. It is thus of future interest to better predict radiation belt fluxes by combining a Kp prediction model. Long-term forecasting is also required to perform a more comprehensive and accurate analysis of our model performance, which will be addressed in future work.

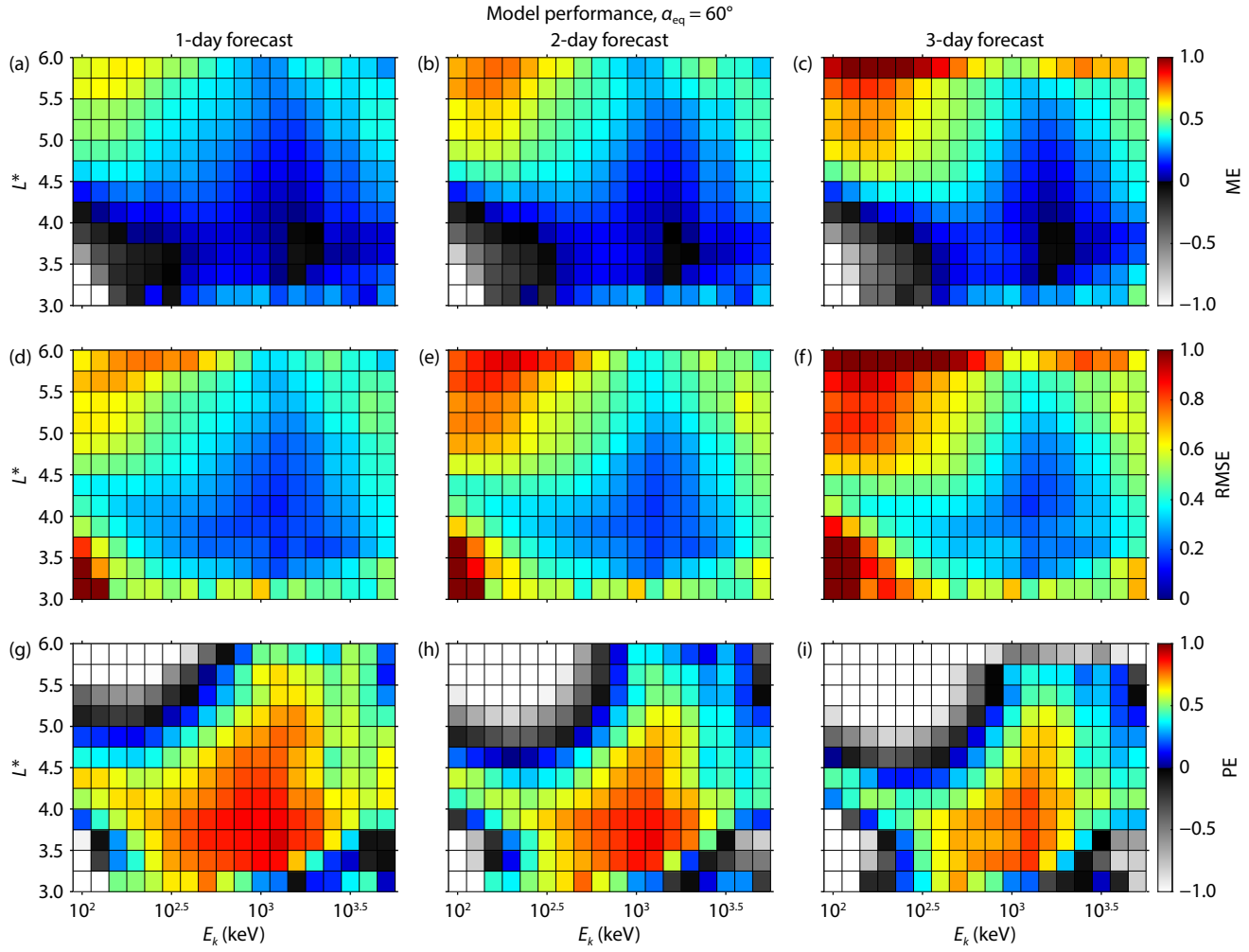

Figure 6. Distribution of the three performance metrics (ME, RMSE, and PE) as a function of electron energy and L^* for $\alpha_{eq} = 60°$ corresponding to 1-, 2-, and 3-day forecasts.

Acknowledgments

This work was supported by the National Natural Science Foundation of China (Grant Nos. 42025404, 42188101, and 42241143), the National Key R&D Program of China (Grant Nos. 2022YFF0503700 and 2022YFF0503900), the B-type Strategic Priority Program of the Chinese Academy of Sciences (Grant No. XDB41000000), and the Fundamental Research Funds for the Central Universities (Grant No. 2042022kf1012). We are grateful to the VAP-ECT group for providing Van Allen Probe electron flux data. All Van Allen Probe data are available from the website (http://www.RBSP-ect.lanl.gov/). We also thank the OMNIWeb service (https://omniweb.gsfc.nasa.gov/) for providing the geomagnetic indices.

References

Baker, D. N., McPherron, R. L., Cayton, T. E., and Klebesadel, R. W. (1990). Linear prediction filter analysis of relativistic electron properties at 6.6 R_E. *J. Geophys. Res.: Space Phys.*, *95*(A9), 15133–15140. https://doi.org/10.1029/ja095ia09p15133

Baker, D. N., Jaynes, A. N., Hoxie, V. C., Thorne, R. M., Foster, J. C., Li, X., Fennell, J. F., Wygant, J. R., Kanekal, S. G., ... Lanzerotti, L. J. (2014). An impenetrable barrier to ultrarelativistic electrons in the Van Allen radiation belts. *Nature*, *515*(7528), 531–534. https://doi.org/10.1038/nature13956

Beutier, T., and Boscher, D. (1995). A three-dimensional analysis of the electron radiation belt by the Salammbô code. *J. Geophys. Res.: Space Phys.*, *100*(A8), 14853–14861. https://doi.org/10.1029/94JA03066

Boynton, R. J., Balikhin, M. A., Sibeck, D. G., Walker, S. N., Billings, S. A., and Ganushkina, N. (2016). Electron flux models for different energies at geostationary orbit. *Space Weather*, *14*(10), 846–860. https://doi.org/10.1002/2016SW001506

Brautigam, D. H., and Albert, J. M. (2000). Radial diffusion analysis of outer radiation belt electrons during the October 9, 1990, magnetic storm. *J. Geophys. Res.: Space Phys.*, *105*(A1), 291–309. https://doi.org/10.1029/1999JA900344

Cao, X., Ni, B. B., Liang, J., Xiang, Z., Wang, Q., Shi, R., Gu, X. D., Zhou, C., Zhao, Z. Y., ... Liu, J. (2016). Resonant scattering of central plasma sheet protons by multiband EMIC waves and resultant proton loss timescales. *J. Geophys. Res.: Space Phys.*, *121*(2), 1219–1232. https://doi.org/10.1002/2015JA021933

Cao, X., Ni, B. B., Summers, D., Zou, Z. Y., Fu, S., and Zhang, W. X. (2017a). Bounce resonance scattering of radiation belt electrons by low-frequency hiss: Comparison with cyclotron and Landau resonances. *Geophys. Res. Lett.*, *44*(19), 9547–9554. https://doi.org/10.1002/2017GL075104

Cao, X., Ni, B. B., Summers, D., Bortnik, J., Tao, X., Shprits, Y. Y., Lou, Y. Q., Gu, X. D., Fu, S., ... Wang, Q. (2017b). Bounce resonance scattering of radiation belt electrons by H^+ band EMIC waves. *J. Geophys. Res.: Space Phys.*, *122*(2), 1702–1713. https://doi.org/10.1002/2016JA023607

Cao, X., Shprits, Y. Y., Ni, B. B., and Zhelavskaya, I. S. (2017c). Scattering of ultra-relativistic electrons in the Van Allen radiation belts accounting for hot plasma effects. *Sci. Rep.*, *7*(1), 17719. https://doi.org/10.1038/s41598-017-17739-7

Cao, X., Ni, B. B., Summers, D., Fu, S., Gu, X. D., and Shi, R. (2020a). Hot plasma effects on the pitch-angle scattering rates of radiation belt electrons due to

plasmaspheric hiss. *Astrophys. J.*, *896*(2), 118. https://doi.org/10.3847/1538-4357/ab9107

Cao, X., Ni, B. B., Summers, D., Shprits, Y. Y., and Lou, Y. Q. (2020b). Effects of polarization reversal on the pitch angle scattering of radiation belt electrons and ring current protons by EMIC waves. *Geophys. Res. Lett.*, *47*(17), e2020GL089718. https://doi.org/10.1029/2020GL089718

Cao, X., Lu, P., Zhu, Q., Ma, X., and Ni, B. B. (2023). Bounce resonance scattering of slot region electrons by plasmaspheric hiss. *Chin. J. Geophys.* (*in Chinese*), *66*(5), 1796–1806. https://doi.org/10.6038/cjg2022Q0669

Capannolo, L., Li, W., Spence, H., Johnson, A. T., Shumko, M., Sample, J., and Klumpar, D. (2021). Energetic electron precipitation observed by FIREBIRD-II potentially driven by EMIC waves: Location, extent, and energy range from a multievent analysis. *Geophys. Res. Lett.*, *48*(5), e2020GL091564. https://doi.org/10.1029/2020GL091564

Carpenter, D. L., and Anderson, R. R. (1992). An ISEE/whistler model of equatorial electron density in the magnetosphere. *J. Geophys. Res.*: *Space Phys.*, *97*(A2), 1097–1108. https://doi.org/10.1029/91JA01548

Chen, Y., Reeves, G. D., Fu, X. R., and Henderson, M. (2019). PreMevE: New predictive model for megaelectron-volt electrons inside Earth's outer radiation belt. *Space Weather*, *17*(3), 438–454. https://doi.org/10.1029/2018SW002095

Coleman, T., McCollough, J. P., Young, S., and Rigler, E. J. (2018). Operational nowcasting of electron flux levels in the outer zone of Earth's radiation belt. *Space Weather*, *16*(5), 501–518. https://doi.org/10.1029/2017SW001788

Daae, M., Shprits, Y. Y., Ni, B., Koller, J., Kondrashov, D., and Chen, Y. (2011). Reanalysis of radiation belt electron phase space density using various boundary conditions and loss models. *Adv. Space Res.*, *48*(8), 1327–1334. https://doi.org/10.1016/j.asr.2011.07.001

de Lima, R. P., Chen, Y., and Lin, Y. Z. (2020). Forecasting megaelectron-volt electrons inside Earth's outer radiation belt: PreMevE 2.0 based on supervised machine learning algorithms. *Space Weather*, *18*(2), e2019SW002399. https://doi.org/10.1029/2019SW002399

Fu, H. S., Cao, J. B., Yang, B., and Lu, H. Y. (2011). Electron loss and acceleration during storm time: The contribution of wave–particle interaction, radial diffusion, and transport processes. *J. Geophys. Res.*: *Space Phys.*, *116*(A10), A10210. https://doi.org/10.1029/2011JA016672

Fu, S., Ni, B. B., Zhou, R. X., Cao, X., and Gu, X. D. (2019). Combined scattering of radiation belt electrons caused by Landau and bounce resonant interactions with magnetosonic waves. *Geophys. Res. Lett.*, *46*(17-18), 10313–10321. https://doi.org/10.1029/2019GL084438

Fu, S., Yi, J., Ni, B. B., Zhou, R. X., Hu, Z. J., Cao, X., Gu, X. D., and Guo, D. Y. (2020). Combined scattering of radiation belt electrons by low-frequency hiss: Cyclotron, Landau, and bounce resonances. *Geophys. Res. Lett.*, *47*(5), e2020GL086963. https://doi.org/10.1029/2020GL086963

Glauert, S. A., Horne, R. B., and Meredith, N. P. (2014). Three-dimensional electron radiation belt simulations using the BAS Radiation Belt Model with new diffusion models for chorus, plasmaspheric hiss, and lightning-generated whistlers. *J. Geophys. Res.*: *Space Phys.*, *119*(1), 268–289. https://doi.org/10.1002/2013JA019281

Godinez, H. C., and Koller, J. (2012). Localized adaptive inflation in ensemble data assimilation for a radiation belt model. *Space Weather*, *10*(8), S08001. https://doi.org/10.1029/2012SW000767

He, F., Yao, Z. H., Ni, B. B., Cao, X., Ye, S. Y., Guo, R. L., Li, J. X., Ren, Z. P., Yue, X. A., Zhang, Y. L., Wei, Y., Zhang, X. X., and Pu, Z. Y. (2023). Sawtooth and dune auroras simultaneously driven by waves around the plasmapause. *Earth Planet. Phys.*, *7*(2), 237–246. https://doi.org/10.26464/epp2023023

Hudson, M. K., Kress, B. T., Mueller, H. R., Zastrow, J. A., and Blake, J. B. (2008). Relationship of the Van Allen radiation belts to solar wind drivers. *J. Atmos. Solar-Terr. Phys.*, *70*(5), 708–729. https://doi.org/10.1016/j.jastp.2007.11.003

Kellerman, A. C., Shprits, Y. Y., and Turner, D. L. (2013). A Geosynchronous Radiation-belt Electron Empirical Prediction (GREEP) model. *Space Weather*, *11*(8), 463–475. https://doi.org/10.1002/swe.20074

Kellerman, A. C., Shprits, Y. Y., Kondrashov, D., Subbotin, D., Makarevich, R. A., Donovan, E., and Nagai, T. (2014). Three-dimensional data assimilation and reanalysis of radiation belt electrons: Observations of a four-zone structure using five spacecraft and the VERB code. *J. Geophys. Res.*: *Space Phys.*, *119*(11), 8764–8783. https://doi.org/10.1002/2014JA020171

Koller, J., Chen, Y., Reeves, G. D., Friedel, R. H. W., Cayton, T. E., and Vrugt, J. A. (2007). Identifying the radiation belt source region by data assimilation. *J. Geophys. Res.*: *Space Phys.*, *112*(A6), A06244. https://doi.org/10.1029/2006JA012196

Kondrashov, D., Shprits, Y., Ghil, M., and Thorne, R. (2007). A Kalman filter technique to estimate relativistic electron lifetimes in the outer radiation belt. *J. Geophys. Res.*: *Space Phys.*, *112*(A10), A10227. https://doi.org/10.1029/2007JA012583

Kondrashov, D., Ghil, M., and Shprits, Y. (2011). Lognormal Kalman filter for assimilating phase space density data in the radiation belts. *Space Weather*, *9*(11), S11006. https://doi.org/10.1029/2011SW000726

Li, L. Y., Yu, J., Cao, J. B., Wang, Z. Q., Yu, Y. Q., Reeves, G. D., and Li, X. (2016). Effects of ULF waves on local and global energetic particles: Particle energy and species dependences. *J. Geophys. Res.*: *Space Phys.*, *121*(11), 11007–11020. https://doi.org/10.1002/2016JA023149

Li, W., Shprits, Y. Y., and Thorne, R. M. (2007). Dynamic evolution of energetic outer zone electrons due to wave–particle interactions during storms. *J. Geophys. Res.*: *Space Phys.*, *112*(A10), A10220. https://doi.org/10.1029/2007JA012368

Ling, A. G., Ginet, G. P., Hilmer, R. V., and Perry, K. L. (2010). A neural network–based geosynchronous relativistic electron flux forecasting model. *Space Weather*, *8*(9), S09003. https://doi.org/10.1029/2010SW000576

Ma, Q., Li, W., Thorne, R. M., Ni, B., Kletzing, C. A., Kurth, W. S., Hospodarsky, G. B., Reeves, G. D., Henderson, M. G., Spence, H. E., ... Angelopoulos, V. (2015). Modeling inward diffusion and slow decay of energetic electrons in the Earth's outer radiation belt. *Geophys. Res. Lett.*, *42*(4), 987–995. https://doi.org/10.1002/2014GL062977

Mauk, B. H., Fox, N. J., Kanekal, S. G., Kessel, R. L., Sibeck, D. G., and Ukhorskiy, A. (2013). Science objectives and rationale for the radiation belt storm probes mission. *Space Sci. Rev.*, *179*(1), 3–27. https://doi.org/10.1007/s11214-012-9908-y

Mei, Y., Ge, Y. S., Du, A. M., Gu, X. D., Summers, D., Li, X. L., Fu, S., and Xiang, Z. (2021). Energy-dependent boundaries of Earth's radiation belt electron slot region. *Astrophys. J.*, *922*(2), 246. https://doi.org/10.3847/1538-4357/ac25ec

Naehr, S. M., and Toffoletto, F. R. (2005). Radiation belt data assimilation with an extended Kalman filter. *Space Weather*, *3*(6), S06001. https://doi.org/10.1029/2004SW000121

Ni, B. B., Thorne, R. M., Shprits, Y. Y., and Bortnik, J. (2008). Resonant scattering of plasma sheet electrons by whistler-mode chorus: Contribution to diffuse auroral precipitation. *Geophys. Res. Lett.*, *35*(11), L11106. https://doi.org/10.1029/2008GLO34032

Ni, B. B., Shprits, Y., Thorne, R., Friedel, R., and Nagai, T. (2009a). Reanalysis of relativistic radiation belt electron phase space density using multisatellite observations: Sensitivity to empirical magnetic field models. *J. Geophys. Res.*: *Space Phys.*, *114*(A12), A12208. https://doi.org/10.1029/2009JA014438

Ni, B. B., Shprits, Y., Nagai, T., Thorne, R., Chen, Y., Kondrashov, D., and Kim, H. J. (2009b). Reanalyses of the radiation belt electron phase space density using nearly equatorial CRRES and polar-orbiting Akebono satellite observations. *J. Geophys. Res.*: *Space Phys.*, *114*(A5), A05208. https://doi.org/10.1029/2008JA013933

Ni, B. B., Bortnik, J., Thorne, R. M., Ma, Q. L., and Chen, L. J. (2013a). Resonant scattering and resultant pitch angle evolution of relativistic electrons by plasmaspheric hiss. *J. Geophys. Res.*: *Space Phys.*, *118*(12), 7740–7751. https://doi.org/10.1002/2013JA019260

Ni, B. B., Shprits, Y. Y., Friedel, R. H. W., Thorne, R. M., Daae, M., and Chen, Y. (2013b). Responses of Earth's radiation belts to solar wind dynamic pressure variations in 2002 analyzed using multisatellite data and Kalman filtering. *J. Geophys. Res.*: *Space Phys.*, *118*(7), 4400–4414. https://doi.org/10.1002/jgra.50437

Ni, B. B., Cao, X., Zou, Z. Y., Zhou, C., Gu, X. D., Bortnik, J., Zhang, J. C., Fu, S., Zhao, Z. Y., ... Xie, L. (2015). Resonant scattering of outer zone relativistic electrons by multiband EMIC waves and resultant electron loss time scales. *J. Geophys. Res.*: *Space Phys.*, *120*(9), 7357–7373. https://doi.org/10.1002/2015JA021466

Ni, B. B., Thorne, R. M., Zhang, X. J., Bortnik, J., Pu, Z. Y., Xie, L., Hu, Z. J., Han, D. S., Shi, R., Zhou, C., and Gu, X. D. (2016). Origins of the Earth's diffuse auroral precipitation. *Space Sci. Rev.*, *200*(1), 205–259. https://doi.org/10.1007/s11214-016-0234-7

Ni, B. B., Hua, M., Zhou, R. X., Yi, J., and Fu, S. (2017). Competition between outer zone electron scattering by plasmaspheric hiss and magnetosonic waves. *Geophys. Res. Lett.*, *44*(8), 3465–3474. https://doi.org/10.1002/2017GL072989

Ni, B. B., Huang, H., Zhang, W. X., Gu, X. D., Zhao, H., Li, X. L., Baker, D., Fu, S., Xiang, Z., and Cao, X. (2019). Parametric sensitivity of the formation of

reversed electron energy spectrum caused by plasmaspheric hiss. *Geophys. Res. Lett.*, *46*(8), 4134–4143. https://doi.org/10.1029/2019GL082032

Ni, B. B., Hua, M., Gu, X. D., Fu, S., Xiang, Z., Cao, X., and Ma, X. (2022). Artificial modification of Earth's radiation belts by ground-based very-low-frequency (VLF) transmitters. *Sci. China Earth Sci.*, *65*(3), 391–413. https://doi.org/10.1007/s11430-021-9850-7

Ni, B. B., Zhang, Y., and Gu, X. D. (2023a). Identification of ring current proton precipitation driven by scattering of electromagnetic ion cyclotron waves. *Fundam. Res.*, *3*(2), 257–264. https://doi.org/10.1016/j.fmre.2021.12.018

Ni, B. B., Summers, D., Xiang, Z., Dou, X. K., Tsurutani, B. T., Meredith, N. P., Dong, J. H., Chen, L. J., Reeves, G. D., ... Xu, W. (2023b). Unique banded structures of plasmaspheric hiss waves in the Earth's magnetosphere. *J. Geophys. Res.: Space Phys.*, *128*(3), e2023JA031325. https://doi.org/10.1029/2023JA031325

Reeves, G. D., Chen, Y., Cunningham, G. S., Friedel, R. W. H., Henderson, M. G., Jordanova, V. K., Koller, J., Morley, S. K., Morley, S. K., Thomsen, M. F., and Zaharia, S. (2012). Dynamic radiation environment assimilation model: DREAM. *Space Weather*, *10*(3), S03006. https://doi.org/10.1029/2011SW000729

Reeves, G. D., Spence, H. E., Henderson, M. G., Morley, S. K., Friedel, R. H. W., Funsten, H. O., Baker, D. N., Kanekal, S. G., Blake, J. B., ... Niehof, J. T. (2013). Electron acceleration in the heart of the Van Allen radiation belts. *Science*, *341*(6149), 991–994. https://doi.org/10.1126/science.1237743

Rigler, E. J., Baker, D. N., Weigel, R. S., Vassiliadis, D., and Klimas, A. J. (2004). Adaptive linear prediction of radiation belt electrons using the Kalman filter. *Space Weather*, *2*(3), S03003. https://doi.org/10.1029/2003SW000036

Schiller, Q., Li, X., Koller, J., Godinez, H., and Turner, D. L. (2012). A parametric study of the source rate for outer radiation belt electrons using a Kalman filter. *J. Geophys. Res.: Space Phys.*, *117*(A9), A09211. https://doi.org/10.1029/2012JA017779

Schulz, M., and Lanzerotti, L. J. (1974). *Particle Diffusion in the Radiation Belts*. Berlin: Springer. https://doi.org/10.1007/978-3-642-65675-0

Shin, D. K., Lee, D. Y., Kim, K. C., Hwang, J., and Kim, J. (2016). Artificial neural network prediction model for geosynchronous electron fluxes: Dependence on satellite position and particle energy. *Space Weather*, *14*(4), 313–321. https://doi.org/10.1002/2015SW001359

Shprits, Y., Kondrashov, D., Chen, Y., Thorne, R., Ghil, M., Friedel, R., and Reeves, G. (2007). Reanalysis of relativistic radiation belt electron fluxes using CRRES satellite data, a radial diffusion model, and a Kalman filter. *J. Geophys. Res.: Space Phys.*, *112*(A12), A12216. https://doi.org/10.1029/2007JA012579

Shprits, Y., Daae, M., and Ni, B. B. (2012). Statistical analysis of phase space density buildups and dropouts. *J. Geophys. Res.: Space Phys.*, *117*(A1), A01219. https://doi.org/10.1029/2011JA016939

Shprits, Y., Kellerman, A., Kondrashov, D., and Subbotin, D. (2013). Application of a new data operator-splitting data assimilation technique to the 3-D VERB diffusion code and CRRES measurements. *Geophys. Res. Lett.*, *40*(19), 4998–5002. https://doi.org/10.1002/grl.50969

Shprits, Y. Y., Subbotin, D., and Ni, B. B. (2009). Evolution of electron fluxes in the outer radiation belt computed with the VERB code. *J. Geophys. Res.: Space Phys.*, *114*(A11), A11209. https://doi.org/10.1029/2008JA013784

Son, J., Moon, Y. J., and Shin, S. (2022). 72-hour time series forecasting of hourly relativistic electron fluxes at geostationary orbit by deep learning. *Space Weather*, *20*(10), e2022SW003153. https://doi.org/10.1029/2022SW003153

Su, Z. P., Xiao, F. L., Zheng, H. N., and Wang, S. (2010). STEERB: A three-dimensional code for storm-time evolution of electron radiation belt. *J. Geophys. Res.: Space Phys.*, *115*(A9), A09208. https://doi.org/10.1029/2009JA015210

Summers, D., and Thorne, R. M. (2003). Relativistic electron pitch-angle scattering by electromagnetic ion cyclotron waves during geomagnetic storms. *J. Geophys. Res.: Space Phys.*, *108*(A4), 1143. https://doi.org/10.1029/2002JA009489

Tang, R. X., Tao, Y. H., Li, J. H., Chen, Z., Deng, X. H., and Li, H. M. (2022). The short-time prediction of the energetic electron flux in the planetary radiation belt based on stacking ensemble-learning algorithm. *Space Weather*, *20*(2), e2021SW002969. https://doi.org/10.1029/2021SW002969

Thorne, R. M., Shprits, Y. Y., Meredith, N. P., Horne, R. B., Li, W., and Lyons, L. R. (2007). Refilling of the slot region between the inner and outer electron radiation belts during geomagnetic storms. *J. Geophys. Res.: Space Phys.*, *112*(A6), A06203. https://doi.org/10.1029/2006JA012176

Thorne, R. M. (2010). Radiation belt dynamics: The importance of wave–particle interactions. *Geophys. Res. Lett.*, *37*(22), L22107. https://doi.org/10.1029/2010GL044990

Thorne, R. M., Li, W., Ni, B., Ma, Q., Bortnik, J., Chen, L., Baker, D. N., Spence, H. E., Reeves, G. D., ... Kanekal, S. G. (2013). Rapid local acceleration of relativistic radiation-belt electrons by magnetospheric chorus. *Nature*, *504*(7480), 411–414. https://doi.org/10.1038/nature12889

Tibocha, A. M. C., de Wiljes, J., Shprits, Y. Y., and Aseev, N. A. (2021). Reconstructing the dynamics of the outer electron radiation belt by means of the standard and ensemble Kalman filter with the verb-3D code. *Space Weather*, *19*(10), e2020SW002672. https://doi.org/10.1029/2020SW002672

Tu, W. C., Cunningham, G. S., Chen, Y., Henderson, M. G., Camporeale, E., and Reeves, G. D. (2013). Modeling radiation belt electron dynamics during GEM challenge intervals with the DREAM3D diffusion model. *J. Geophys. Res.: Space Phys.*, *118*(10), 6197–6211. https://doi.org/10.1002/jgra.50560

Wang, C. Q., Zhang, X. G., Shen, G. H., Zhang, S. Y., Zhang, X. X., Huang, C., and Li, X. J. (2021). Dynamic results of electron flux in radiation belt from 2011 to 2015 based on FY-3B satellite observation. *Chin. J. Geophys.* (*in Chinese*), *64*(6), 1831–1841. https://doi.org/10.6038/cjg2021O0341

Wang, J. H., Guo, D. Y., Xiang, Z., Ni, B. B., Liu, Y. X. Z., and Dong, J. H. (2023). Prediction of geosynchronous electron fluxes using an artificial neural network driven by solar wind parameters. *Adv. Space Res.*, *71*(1), 275–285. https://doi.org/10.1016/j.asr.2022.10.013

Wei, L. H., Zhong, Q. Z., Lin, R. L., Wang, J. J., Liu, S. Q., and Cao, Y. (2018). Quantitative prediction of high-energy electron integral flux at geostationary orbit based on deep learning. *Space Weather*, *16*(7), 903–916. https://doi.org/10.1029/2018SW001829

Wing, S., Turner, D. L., Ukhorskiy, A. Y., Johnson, J. R., Sotirelis, T., Nikoukar, R., and Romeo, G. (2022). Modeling radiation belt electrons with information theory informed neural networks. *Space Weather*, *20*(8), e2022SW003090. https://doi.org/10.1029/2022SW003090

Xiang, Z., Tu, W. C., Li, X. L., Ni, B. B., Morley, S. K., and Baker, D. N. (2017). Understanding the mechanisms of radiation belt dropouts observed by Van Allen Probes. *J. Geophys. Res.: Space Phys.*, *122*(10), 9858–9879. https://doi.org/10.1002/2017JA024487

Xiang, Z., Tu, W. C., Ni, B. B., Henderson, M. G., and Cao, X. (2018). A statistical survey of radiation belt dropouts observed by Van Allen Probes. *Geophys. Res. Lett.*, *45*(16), 8035–8043. https://doi.org/10.1029/2018GL078907

Xiao, F. L., Yang, C., He, Z. G., Su, Z. P., Zhou, Q. H., He, Y. H., Kletzing, C. A., Kurth, W. S., Hospodarsky, G. B., ... Wygant, J. R. (2014). Chorus acceleration of radiation belt relativistic electrons during March 2013 geomagnetic storm. *J. Geophys. Res.: Space Phys.*, *119*(5), 3325–3332. https://doi.org/10.1002/2014JA019822

Xiao, F. L., Zhou, Q. H., He, Y. H., Yang, C., Liu, S., Baker, D. N., Spence, H. E., Reeves, G. D., Funsten, H. O., and Blake, J. B. (2015). Penetration of magnetosonic waves into the plasmasphere observed by the Van Allen Probes. *Geophys. Res. Lett.*, *42*(18), 7287–7294. https://doi.org/10.1002/2015GL065745

Yu, Y., Koller, J., Jordanova, V. K., Zaharia, S. G., and Godinez, H. C. (2014). Radiation belt data assimilation of a moderate storm event using a magnetic field configuration from the physics-based RAM-SCB model. *Ann Geophys.*, *32*(5), 473–483. https://doi.org/10.5194/angeo-32-473-2014

Zhang, D. J., Liu, W. L., Li, X. L., Sarris, T. E., Wang, Y. F., Xiao, C., Zhang, Z., and Wygant, J. R. (2020). Relation between shock-related impulse and subsequent ULF wave in the Earth's magnetosphere. *Geophys. Res. Lett.*, *47*(23), e2020GL090027. https://doi.org/10.1029/2020GL090027

Zhang, H., Fu, S. Y., Xie, L., Zhao, D., Yue, C., Pu, Z. Y., Xiong, Y., Wu, T., Zhao, S. J., ... Luo, Z. K. (2020). Relativistic electron flux prediction at geosynchronous orbit based on the neural network and the quantile regression method. *Space Weather*, *18*(9), e2020SW002445. https://doi.org/10.1029/2020SW002445

Zhu, J. N., Guo, J. G., Ni, B. B., Cao, X., Xiang, Z., Fu, S., Gu, X. D., and Ma, X. (2021). Multi-dimensional data assimilation and analyses of Earth's outer electron radiation belt. *Chin. J. Geophys.* (*in Chinese*), *64*(5), 1496–1507. https://doi.org/10.6038/cjg2021O0489

Zhu, M. H., Yu, Y. Q., Cao, X., Ni, B. B., Tian, X. B., Cao, J. B., and Jordanova, V. K. (2022). Effects of polarization-reversed electromagnetic ion cyclotron waves on the ring current dynamics. *Earth Planet. Phys.*, *6*(4), 329–338. https://doi.org/10.26464/epp2022037

Zong, Q. G., Rankin, R., and Zhou, X. Z. (2017). The interaction of ultra-low-frequency Pc3-5 waves with charged particles in Earth's magnetosphere. *Rev. Mod. Plasma Phys.*, *1*, 10. https://doi.org/10.1007/s41614-017-0011-4